

# A Joint Imaging and Comparison Technique of Distributed Acoustic

1

## Sensing and Geophone Data

2

**Samir F. Jreij, Whitney J. Trainor-Guitton, and James L. Simmons**

3

Colorado School of Mines,

4

1500 Illinois Ave,

5

Golden, CO, 80401

6

(August 3, 2018)

7

**Running head: A Joint Imaging and Comparison Technique of Distributed Acoustic Sensing  
and Geophone Data**

8

## ABSTRACT

9 The PoroTomo survey at Brady's Natural Lab consisted of 238 multi-component geophones that  
10 are spaced anywhere from 60 to 150 meters apart. This proves to be a difficult migration problem  
11 with such sparse spacing. An imaging technique that utilizes both multi-component geophones  
12 and a surface distributed acoustic sensor (DAS) acquisition attempts to resolve the spatial sampling  
13 issue. Fortunately, the PoroTomo survey consisted of surface DAS cable with a 1-meter receiver  
14 spacing along the fiber. Both 2D and 3D numerical experiments test the feasibility of using the  
15 broadside sensitive multi-component geophones and the densely sampled DAS data together to  
16 minimize insensitivity to certain waves. The objective of these experiments are to analyze if the  
17 densely sampled DAS fiber data can help improve the image produced by the sparsely sampled  
18 geophones. In 2D, a reflectivity model is created from the local fault model in the PoroTomo Survey.  
19 Quantitative analysis provides an unbiased comparison of the results. The quantitative analysis  
20 utilizes a convolutional neural network to prove that DAS adds value to imaging efforts. A more

21 challenging example in 3D confirms the conclusions made in 2D. A methodology to model DAS  
22 data in 3D shows that utilizing DAS in surface surveys with sparse, multi-component geophones  
23 proves to be useful in improving the classification accuracy of the image. The results, however,  
24 are inconclusive because the migrated images are too low of a frequency to analyze due to the  
25 limitation of the velocity model. Lessons learned from the data collected at the PoroTomo survey  
26 and the numerical experiments are that a more regular acquisition geometry of the horizontal DAS  
27 fiber increases identifying the true reflectors.

## INTRODUCTION

28 Distributed acoustic sensing (DAS) is a technology that uses Rayleigh scattering in a fiber-optic ca-  
29 ble to detect elastic signals **data** when wave particle motion is parallel to the sensing fiber (Hornman  
30 et al., 2013). The two main components used in distributed sensing are the interrogator unit and the  
31 fiber-optic cable. The interrogator unit works as a light source and receiver. It sends a known pulse  
32 of light down the fiber. Nearly any type of existing fiber-optic cable can be used in conjunction  
33 with an interrogator unit. Small imperfections within the fiber cause backscattering of light. Strain  
34 events along the fiber cause this backscattering to change slightly when a wavefield approaches the  
35 fiber. The interrogator unit can measure the Rayleigh backscattering and relate it to the strain along  
36 the fiber.

37 **DAS Advantages**

38 **DAS Disadvantages**

39 Although DAS may seem like the solution to seismic acquisition, it also has many disadvantages.  
40 DAS is most sensitive to waves that have particle motion parallel to the orientation of the fiber, so  
41 it is said that the technology has broadside insensitivity. Multi-component geophones also have this  
42 issue; with more recording components, however, they are able to resolve more of the wavefield and  
43 are not affected by this broadside insensitivity as much.

44 Another disadvantage is that DAS coupling is not trivial in all environments. In a borehole  
45 environment, DAS can be cemented behind casing or permanently installed on production tubing  
46 (Mateeva et al., 2013). Surface distributed sensor coupling is a more challenging issue. Lindsey  
47 et al. (2017) describe how fibers can be utilized in loosely coupled environments. The Stanford

48 Fiber Optic Array consists of a 2.5 km long array that lies in a conduit about 1 to 2 meters below  
49 ground. The DAS fiber geometry is restricted by the conduits, though, and the task of installing the  
50 fiber is more difficult if there are no existing conduits. Daley et al. (2013) have trenched the cable  
51 and returned at a later time to shoot the seismic survey. Although this method is effective, waiting  
52 to shoot a survey at a later time can be inconvenient.

53 **Previous Work**

54 Historically, DAS has been used in a borehole environment for flow monitoring, temperature mea-  
55 surements, and vertical seismic profiles (Clarke and Sandberg, 1983; Krohn et al., 2000; Mestayer  
56 et al., 2011; Barberan et al., 2012; Cox et al., 2012; Daley et al., 2013; Mateeva et al., 2014).

57 Mestayer et al. (2011) describe how permanently installed fiber-optic infrastructure in existing  
58 wells can enable low-cost non-intrusive geophysical monitoring. Geophones generally only acquire  
59 data along a short subset of the well due to the limited number of receivers at predetermined receiver  
60 spacing in VSP receiver arrays. This makes repeatable time-lapse surveys difficult as placing the  
61 geophones in the same location is not trivial. Mestayer et al. (2011) also discuss how borehole  
62 DAS is able to improve repeatability and time-lapse sensitivity because it is able to acquire data  
63 along the full well with a single shot. Mateeva et al. (2014) also describe a time lapse, 3D DAS  
64 VSP application. They conclude that DAS has many major business impacts on fields that require  
65 enhanced oil recovery (EOR) including cost efficiency, safety, and synergy with other fiber optic  
66 applications.

67 Barberan et al. (2012) discuss different ways DAS fiber can be coupled in a borehole environ-  
68 ment. DAS fiber can be clamped to production tubing and used as a downhole seismic sensor.  
69 Barberan et al. (2012) expand on this explaining that acquiring seismic data over the entire well is

70 essential for acquiring additional transit times for velocity inversion and it allows for a wide range  
71 of incidence angles in terms of wave directions that arrive at the fiber for inversion.

72 Daley et al. (2013) describes field tests from both horizontal and borehole distributed sensors.  
73 They conclude that the signal-to-noise (SNR) in surface DAS is not sufficient for observing P-waves  
74 and that DAS is more useful in borehole environments or longer surface arrays. They don't go into  
75 detail, however, regarding why certain waves are not observable in DAS.

76 As seen in these examples, DAS research has emphasized acquiring data in borehole environ-  
77 ments because many wells are already equipped with fiber for production. As a result, acquiring  
78 DAS in boreholes is as simple as connecting the existing fiber-optic cable to a new interrogator unit  
79 that senses acoustic signal **data**. Although there are some studies on surface DAS acquisitions (Da-  
80 ley et al., 2013; Hornman, 2017), there has not been a thorough study in active source experiments.

81 Daley et al. (2013) experiment with a vertical vibrator (vertical-force) source. The reflected  
82 P-wave is not recorded on the DAS fiber as the experiment only had 1,000 meters of offset, and,  
83 therefore, the authors concluded that the SNR in surface DAS is insufficient for observing P-waves  
84 due to the relatively small incidental reflected angle. Other source mechanisms must be investigated  
85 before such a conclusion can be made about the feasibility of using surface DAS fiber. Another  
86 option is utilizing the DAS fiber along with geophones to attempt to minimize the insensitivity of  
87 some waves. This paper explores different imaging experiments using the field geometry from the  
88 PoroTomo survey in Northwest Nevada and numerical modeling to explain how DAS fiber can help  
89 minimize the insensitivity to waves in conjunction with geophones. The objective of these experi-  
90 ments is to analyze if the densely sampled DAS fiber data can help improve the image produced by  
91 the sparsely sampled geophones.

92 **PoroTomo Survey**

93 The PoroTomo survey involved four-weeks of data acquisition of geodesy, interferometric syn-  
94 thetic aperture radar (InSAR), hydrology, temperature sensing, passive source seismology, and ac-  
95 tive source seismology data (Feigl, 2017; Cardiff et al., 2018). The variety of data that were col-  
96 lected at the PoroTomo survey lead to the origin of the experiments name: Poroelastic Tomography  
97 by Adjoint Inverse Modeling of Data from Seismology, Geodesy, and Hydrology (or PoroTomo for  
98 short). These data were jointly collected to characterize and monitor changes in the rock mechanical  
99 properties of Brady's Natural Laboratory (BNL), an Enhanced Geothermal System (EGS) reservoir.

100 This paper investigates the active seismic source component of the PoroTomo Experiment. The  
101 PoroTomo survey is one of the most unique seismic acquisitions for surface DAS fiber. The survey  
102 included 238 multi-component geophones, 156 three-component (vertical and orthogonal horizon-  
103 tal) vibroseis source locations that swept from 5 to 80 Hz in 20 seconds, 300 meters of borehole  
104 DAS, and nearly nine kilometers of surface fiber-optic cable. The full survey geometry is shown in  
105 Figure 1. As seen in Figure 1, the geophones are sparsely spaced with an average inline spacing of  
106 80 meters. This paper focuses on identifying a methodology to resolve the spatial sampling issue.  
107 The objective of this paper is to identify if the densely sampled DAS data can help improve the  
108 image produced by the sparsely sampled geophones. Both 2D and 3D numerical experiments are  
109 performed to test the feasibility of using the broadside sensitivity of multi-component geophones  
110 and the dense sampling DAS data together to minimize insensitivity to certain waves.

## FIBER SENSITIVITY

111 Understanding how DAS fiber works is essential to working with the data that are currently available  
112 and to design effective future surveys. For a conventional DAS seismic survey, a known pulse of

113 light is sent into the fiber using an interrogator unit and some of the light is naturally scattered back  
114 due to imperfections within the fiber. The interrogator unit is able to record this scattered light along  
115 the fiber up to 10-kilometers away. This is known as the base condition inside of the fiber. The fiber  
116 undergoes a strain when a seismic wavefield approaches and a scattering of light is produced that  
117 is different from the base condition interacts with it, which produces a scattering of light that is  
118 different from the base condition. The interrogator unit is able to relate this new scattering of light  
119 to local strain along the fiber by recording the time of arrival and the phase-lag of the returning light  
120 signals (Parker et al., 2014).

121 DAS fiber is most sensitive to waves that are able to stretch and squeeze the fiber, so the waves  
122 have to have particle motion parallel to the orientation of the fiber. Every seismic sensor has its own  
123 distinct sensitivity to the various types of waves depending on their emergent angle. The emergent  
124 angle ( $\theta$ ) represents the angle between the incoming wave and the surface of the Earth. Consider a  
125 plane wave reflection in the X-Z plane: an emergent angle of  $0^\circ$  represents a wave arriving parallel  
126 to the surface (or a plane wave traveling in the Z-direction); an emergent angle of  $90^\circ$  represents a  
127 wave arriving perpendicular to the surface (or a plane wave traveling in the X-direction).

128 These points can be demonstrated with a simple 2D example. Consider wave propagation in  
129 the X-Z plane in a homogeneous, flat-layered, isotropic or vertical transverse isotropic medium  
130 (Figure 2a-2b). The horizontal DAS fiber is oriented in the x-direction. P-waves have particle  
131 motion parallel to the direction of wave propagation (Aki and Richards, 1980). Normal-incidence  
132 reflections from a horizontal reflector will arrive perpendicular to the surface fiber. Data will not  
133 be seen at short offsets in the case of a reflected P-wave (Figure 2a). The particle motion of P-  
134 waves is parallel to the direction of propagation, so at short offsets, the reflected P-wave will arrive  
135 perpendicular to the fiber. As seen in Figure 3a, P-waves with a  $0^\circ$  emergent angle show zero  
136 amplitude on the fiber and maximum amplitude on the z-component of a geophone, following a

137  $\cos^2(\theta)$  decay with emergent angle ( $\theta$ ). Moving to further offsets yields emergent angles that are  
138 at a larger angle to the fiber. According to Figure 3a, these waves will show more data than waves  
139 arrive perpendicular to the fiber as they are propagating in the direction of the fiber and will show  
140 less data on the vertical component of the geophone. The further the offset, however, the lower the  
141 amplitude of the wave due to attenuation effects.

142 Shear-waves are potentially more interesting when recording with horizontal fiber. Consider  
143 again 2D wave propagation in the X-Z plane in a homogeneous, flat-layered, isotropic or vertical  
144 transverse isotropy medium (Figure 2b). SV-waves have particle motion in the X-Z plane, as do  
145 P-waves (Aki and Richards, 1980). Normal-incidence reflections from a horizontal reflector will  
146 arrive perpendicular to the surface fiber. P-wave particle motion, as stated previously, will be in  
147 the z direction, and consequently, will not be recorded by the fiber. SV wave particle motion will  
148 be in the x-direction (emergent angle of  $0^\circ$ ), and the DAS response will be maximum (Figure 3b).  
149 At larger offsets, the SV-wave emerging angle begins to approach  $90^\circ$ . A larger emerging angle  
150 means less signal data (Figure 3b) is recorded by both the surface DAS and the x-component  
151 of the geophone because the SV-wave particle motion is in the vertical perpendicular to the fiber  
152 (Figure 2b).

153 We also consider using SH-waves with the same 2D survey geometry (homogeneous, flat-  
154 layered, isotropic). S-H waves have particle motion perpendicular to the direction of wave propa-  
155 gation or, in this case, in the y-direction. The DAS response to SH-waves will be zero since the SH  
156 particle motion is perpendicular to the DAS fiber, in the y-direction. In this 2D case, the SH-wave  
157 will be out of plane regardless of source-receiver offset. In 3D, SH-waves can be seen on the DAS  
158 if they are properly oriented. For example, a source-receiver azimuth perpendicular to the 2D fiber  
159 (in this case, in the y-direction) will produce a maximum amplitude reflection on the DAS since  
160 the particle motion is in the x-direction for all offsets. As the source-receiver azimuth moves inline

161 with the fiber, the SH-wave particle motion decreases, and is equal to zero when the source-receiver  
162 azimuth is inline with the fiber.

163 In this section, DAS fiber directionality was described analytically and depicted graphically.  
164 The directionality is important to understand when creating a seismic survey geometry to assist  
165 with geophone deficiencies.

## 2D NUMERICAL MODELING EXAMPLES

166 Imaging the geophone data is a difficult task in the PoroTomo Survey due to the irregular spatial  
167 sampling and offset. This paper focuses on identifying a way to resolve the spatial sampling issue.  
168 Fortunately, the PoroTomo survey includes surface DAS cable that has 10-meter gauge-length and  
169 an equivalent of 1-meter receiver spacing along the fiber. Many papers in the literature are interested  
170 in methods to convert DAS measurements (strain or strain rate) to a geophone equivalent (particle  
171 velocity or displacement) with the intent to replace point sensors with distributed sensors, or use  
172 existing geophone processing to clean up DAS data (Daley et al., 2013, 2015; Jreij et al., 2017).  
173 The idea of using both data types in simultaneous imaging is explored in this paper to produce more  
174 detailed images using synthetic examples.

175 **2D Synthetic Design**

176 Siler and Faulds (2013) mapped the faults of Brady's Natural Lab shown in Figure 4. It is important  
177 to image these faults in detail as they are driving factors behind the recharge of the geothermal  
178 reservoir (Feigl, 2017; Folsom et al., 2018). A slice is taken from the Brady's Natural Lab fault  
179 model (Siler and Faulds, 2013) in the PoroTomo Survey and used as a reflection velocity models.  
180 This slice is shown in Figure 5. The Siler and Faulds (2013) fault model slice is used as a reflectivity

181 model as it contains a variety of structural dips.

182 Seismic sources in the PoroTomo experiment are not on a uniform grid. In fact, the source  
183 spacing is as large as 150 meters. Seismic illumination describes how much of the subsurface can  
184 be imaged given a source-receiver geometry and velocity model. Illumination in seismic surveys  
185 is highly influenced by source-receiver spacing. For the purpose of this section, a constant source  
186 spacing of 75 meters (which is about the average source spacing in the PoroTomo survey) is used  
187 to minimize migration artifact effects from poor illumination. For the 2D experiments present in  
188 this paper, both vertical and horizontal force sources are modeled to represent a vertically and a  
189 horizontal vibe, respectively, which were also collected at BNL for the PoroTomo field experiment.

190 Reverse time migration (RTM) is the imaging technique that is used for the experiments in this  
191 paper. 2D elastic forward modeling is used to produce strain (as measured by DAS) and displace-  
192 ment (as measured by geophones) data along the surface of our 2D example excited by a vertical  
193 force source. Receivers at every one meter across the experiment are used for recording. As seen  
194 in Figure 1, the PoroTomo survey did not include a straight fiber that was this long. It did include,  
195 however, a maximum offset of 1,500-meters across the entire survey. A 2D line of 1,500 meters was  
196 utilized to gather data with similar offsets as the PoroTomo survey.

197 The code generated for these experiments outputs both strain and displacement at every receiver  
198 location. The average geophone spacing is about 70 meters in the PoroTomo experiment. A geo-  
199 phone spacing of 100 meters is chosen to analyze geophone spacing closer to the extremes of this  
200 experiment. The recorded data are generated from a reflectivity model that is derived from Brady's  
201 fault model using an elastic finite difference modeling (FDM) operator from the Madagascar pack-  
202 age (Fomel et al., 2013). The next step is to back propagate the recorded data from this forward  
203 modeling to recover the receiver wavefield. If this was a field experiment, the field data would be

204 back propagated. Two different sources are needed to create the receiver wavefield. An acceleration  
205 force is used for back propagation of the geophone data and a stress tensor is used for back propaga-  
206 tion of the DAS data. The proper way to do imaging is to back propagate the two data types (strain  
207 and displacement) simultaneously, but this was not possible with current codes, so the data are back  
208 propagated individually.

209 The last wavefield that needs to be generated is the source wavefield. The source wavefield is a  
210 forward model from the original source location through a smooth velocity model. It is important  
211 that the velocity model is smooth as reflections will cause an improper final image. Now, a source  
212 and two receiver wavefields exist. An imaging condition is required to combine the wavefields.

213 Traditionally, the zero-lag, cross correlation imaging condition (IC) is used to create a migrated  
214 image (Claerbout, 1985). Although this methodology may provide a solution for elastic imaging,  
215 this IC produces four resulting images (PP, PS, SP, SS). This proves to be a more difficult compari-  
216 son between different data types for the purpose of this paper. Rocha et al. (2016) describes the use  
217 of an energy-norm based IC that exploits wavefield directionality to create a single elastic image  
218 that represents the measure of reflected energy. There are many other benefits to using the energy-  
219 norm IC, but most important for this work is that one final image allows for an easy comparison of  
220 migrated elastic data.

221 The image produced from the elastic energy norm RTM with sparsely sampled multi-component  
222 geophones using a vertical force is shown in Figure 6a. This image shows reflectors are disconti-  
223 uous and difficult to follow. The image is also covered with migration artifacts due to insufficient  
224 sampling of the wavefield. An example of this is presented around 800 meters on the x-axis of  
225 Figure 6a: the migration artifacts make it difficult for an interpreter to follow the shallow reflector.  
226 The deeper reflector in Figure 6a is impossible to identify.

227 The image produced from the elastic energy norm RTM with DAS fiber along the surface of the  
228 model creating a virtual receiver at every one meter is shown in Figure 6b. The shallow reflector in  
229 this image is sharp and continuous, allowing for easy interpretation. Although migration artifacts  
230 are still present around 800 meters on the x-axis, these are different from those experienced in  
231 Figure 6a. These migration artifacts are now due to fake modes present because the wavefield is  
232 extrapolated using only the x-component data that was recorded with DAS fiber.

233 Now there are two images with two different migration artifacts (i.e. types of noise). Stacking  
234 the images should theoretically reduce the noise and highlight the reflection events. Linearly stack-  
235 ing the events, however, will not currently work as the amplitudes are on different scales. Instead,  
236 the amplitudes of both images are normalized by the maximum and then stacked to produce Fig-  
237 ure 6c. Although Figure 6c still has artifacts in it, the reflectors are enhanced and the image is easier  
238 to interpret than Figure 6a or Figure 6b.

239 Fiber attributes were discussed earlier in this paper. Different source types can generate different  
240 polarizations of reflection events. For this reason, the second 2D experiment uses the same geometry  
241 and model as the first experiment, but now an horizontal force is used to generate data. The image  
242 produced from elastic energy norm RTM with sparsely sampled multi-component geophones and  
243 a horizontal force is shown in Figure 7a. This image still shows some discontinuity in reflectors,  
244 but the reflector is much easier to follow. The receiver sampling was not changed, so the image is  
245 still covered with migration artifacts due to insufficient sampling of the wavefield. On the left-hand  
246 side of the geophone image, the end of the dipping fault is not properly imaged. This is due to  
247 insufficient aperture in the migration. The deeper reflector is now easier to identify in Figure 7a.

248 The image produced from elastic energy norm RTM with DAS data and an S-source is shown  
249 in Figure 7b. The DAS image is still very sharp, but now the migration artifacts have diminished.

250 The deeper reflector is much easier to observe and interpret as well. This image is sharp because the  
251 zero-offset SV-wave reflections are perfectly polarized to show the reflectors on DAS and the DAS  
252 data is really well sampled [the DAS data are sampling the Earth response well].

253 There are two images with two different migration artifacts (i.e. types of noise), so the images  
254 are normalized and stacked just as it was done for the previous example. The results are shown in  
255 Figure 7c. Figure 7c shows both reflectors clearer than Figure 6c which suggests that a horizontal  
256 force is more beneficial for near-offset DAS surveys.

257 **Value of Information**

258 All of the experiments presented in the paper can be qualitatively analyzed and discussed, but quali-  
259 tative analysis is always different between people due to different biases and perspectives. A method  
260 to quantitatively analyze the experiments is needed to do effective comparisons.

261 The Value of Information (VOI) is a quantitative tool that originates from the field of decision  
262 analysis to quantify how relevant and reliable an information source is (Trainor-Guitton et al., 2013).  
263 VOI estimates the possible increase in expected utility by gathering information. It is calculated by  
264 comparing the prior value ( $V_{prior}$ , the average utility of a decision made with current information)  
265 to the value with imperfect information ( $V_{imperfect}$ ) by subtracting the two, shown in Equation 1.

$$VOI = V_{imperfect} - V_{prior} \quad (1)$$

266 The goal of this project is to observe if there is any added value to using distributed acoustic  
267 sensing in surface acquisitions. The value with imperfect information shown in Equation 2 can only  
268 be calculated with a quantitative measure of how accurate the information source as,

$$V_{imperfect} = \sum_{j=F,NF} Pr(\theta^{int} = \theta_j) \max_a [ \sum_{i=F,NF} Pr(\theta = \theta_i | \theta^{int} = \theta_j) v_a(\theta_i) ] \quad (2)$$

269 This quantitative measure can be represented by the posterior probability,  $Pr(\theta = \theta_i | \theta^{int} = \theta_j)$ ,  
 270 within the value with imperfect information (Equation 2). Specifically for these problems, the  
 271 posterior probability can be how often interpretations of faults align with the actual presence of  
 272 faults. It is important to calculate the posterior reliability so the value of imperfect information can  
 273 be completed. The posterior probability can be calculated using Equation 3,

$$Pr(\theta = \theta_i | \theta^{int} = \theta_j) = \frac{(Pr(\theta = \theta_i)) Pr(\theta^{int} = \theta_j | \theta = \theta_i)}{Pr(\theta^{int} = \theta_i)}; \forall i, j = F, NF \quad (3)$$

274 where  $\theta$  represents a true value of Fault or Not Fault,  $\theta^{int}$  represents an interpreted Fault or Not  
 275 Fault. There are a variety of methodologies to produce information about whether an interpreted  
 276 fault is actually a fault or not. This paper utilizes a machine learning approach to interpret the  
 277 features in the migrated image.

## 278 Convolutional Neural Network Analysis

279 Machine learning is a field within computer science that focuses on the ability of computer systems  
 280 to learn patterns within data without being explicitly programmed for these patterns (Samuel, 1959).  
 281 Machine learning has had a large boom in the geophysics industry within the last 10 years.

282 There are a variety of machine learning algorithms that can be utilized based on the problem that  
 283 needs to be solved. One of the most powerful machine learning algorithms is the neural network.  
 284 Neural networks are inspired by the biological neural networks that constitute human brains or at  
 285 least how humans perceive they work (Gerven and Bohte, 2018). They consist of many layers in

286 parallel and every layer consists of a number of nodes. All neural networks consists of at least two  
287 layers: the input layer and output layer. All the extra layers in between the input and output layers  
288 are the hidden layers. The nodes of every layer are like neurons in the brain. Every neuron has its  
289 own activation function that determines whether it should be “fired” or not similar to how a neuron  
290 in the brain behaves. Each layer receives the output from the previous layer based on if the previous  
291 neuron is fired or not.

292 Convolutional Neural Networks (CNN) in particular are at the core of most state-of-the-art com-  
293 puter vision solutions for a wide variety of tasks. One of the most accurate CNN image classifiers  
294 is the Inception-v3 model (Szegedy et al., 2015). The original Inception-v3 model is trained and  
295 tested on the 2012 ImageNet Large Scale Visual Recognition Challenge (Russakovsky et al., 2015).  
296 The training dataset consisted of 10,000,000 labeled images that depicted 1,000 object categories.  
297 The Inception-v3 model was able to perform with 3.5% top-5 error, meaning that the target label  
298 is within the top-5 probability classifications that the algorithm produced. A top-5 error of 3.5%  
299 means the Inception-v3 model is able to perform with high accuracy, making it a top contender for  
300 a geophysics image classification problem.

301 The Inception-v3 model utilizes transfer learning which means it stores knowledge gained from  
302 training on the ImageNet dataset and then applies it to a different but related problem. It is difficult to  
303 train a CNN from scratch because a large dataset is needed with a substantial amount of computers  
304 equipped with GPU’s. Instead, the intermediate layers of the Inception-v3 model are used as they  
305 are already trained on detecting edges, shapes, and other high level features. The weights of the  
306 model’s last layer are recreated to identify if an image is either a fault or not a fault.

307 The Inception v3 model’s ability to identify features can be leveraged within the geophysics  
308 realm. The first step is to create some training data to retrain the model. The objective is to see

309 if DAS helped identify more faults than a sparse array of multi-component geophones. For the  
310 experiments in this chapter, RTM images are created from 2D reflectivity slices of the Siler and  
311 Faulds (2013) fault model. There are about 500 other slices along both the X and Y axis of the  
312 PoroTomo grid. A number of these slices can be migrated to create training data for identifying  
313 faults.

314 The next step is to take spatial windows of the migrated images and label them based on if there  
315 are faults or not within the image. 100 meter by 100 meter (10 grid cell by 10 grid cell) subsets of  
316 the migrated images were created. There are a large amount of data present and individually picking  
317 whether an image contains a fault or not would be time consuming. As stated earlier, the true fault  
318 model exists to compare with the migrated images. The same subset of the migrated images can  
319 be compared with the reflectivity model. If more than half the pixels are a fault, then the program  
320 labels the training data as a fault (Figure 8a). Otherwise, the program labels the training data as not  
321 a fault (Figure 8b).

322 This is an easy and automatic way to generate training data, but training is an essential step  
323 prior to testing, so it needs to be continually improved. The next step is to QC the training data to  
324 make sure that the examples are actually of “faults” and “not faults”. Many iterations are required  
325 until an acceptable cross-validation accuracy is achieved. A total of 2500, 100 meter by 100 meter  
326 windowed RTM images were used to train the CNN to detect faults. A final training validation  
327 accuracy of 94.4% is achieved. This is an acceptable accuracy check and now the neural network is  
328 ready to be tested on data that were not included in the training data.

329 A 100 meter by 100 meter testing data is **are** created the same way the training data is **are**  
330 created. The testing data is **are** kept hidden from the training data. The first RTM image that is used  
331 for testing is the vertical source data from the velocity model shown in Figure 5. The first test is

332 on the sparse, multi-component geophone image (Figure 6a). The RTM image is decomposed into  
333 3,625 (100 meter x 100 meter) images with labels of “Faults” and “Not Faults”. This same process  
334 is used for the synthetic created from DAS and multi-component geophones.

335 A posterior reliability of information can be calculated with the results from the testing data.  
336 The resulting posterior reliability of information is shown graphically in Figure 9a and Figure 9b  
337 for a vertical force and a horizontal force, respectively.

338 The results from Figure 9a for the vertical source show that adding DAS into the sparse array  
339 of geophones with Figure 5 as the velocity model improves the classification of faults by 20%.  
340 However, there is an increase in false negatives by about 30%. This means either the normalized,  
341 stacked image has many artifacts or the classifier needs to be better trained on what is not a fault.  
342 The number of false positives decreases by 20% which is a substantial amount. Lastly, the number  
343 of true negatives decreases by almost 30%. This confirms that the classifier needs to be better trained  
344 on what is not a fault.

345 The results from Figure 9b for the horizontal source show that adding DAS into the sparse array  
346 of geophones with Figure 5 as the velocity model decreases the classification of faults by about 1%.  
347 However, the classification of true negatives increases by about 5% and false negatives decreases by  
348 about 5% meaning the DAS data did add some value to the CNN classification.

349 **2D Summary**

350 This section discussed in great detail how 2D DAS data can be modeled. It also showed how a  
351 long offset, 2D surface DAS line can produce a sharp resulting image. A quantitative analysis using  
352 a machine learning methodology showed that DAS does add value to sparse geophone arrays. A  
353 quantitative analysis also shows that using a horizontal force with DAS allows for sharper images.

354 These hypotheses must now be confirmed with a 3D acquisition.

### 3D NUMERICAL MODELING EXAMPLES

355 The objective of this paper is to observe if there is any added value of using surface DAS with  
356 sparsely sampled arranged, multi-component geophones. In the previous section, we observed that  
357 in a long 2D line, there is added value using DAS to help with the spatial sampling. In 3D, however,  
358 there are many more complications than in 2D. This section explores additional examples of using  
359 DAS in combination with multi-component geophones, but now with the PoroTomo 3D survey  
360 geometry. These examples utilize numerical modeling to understand more about what is recorded.

361 A velocity model from sweep interferometry shown in Figure 10 was used to create data (Matzel  
362 et al., 2017a). As in the previous section, a modified version of the conventional elastic FDM code  
363 (ewefdm) present in Madagascar (Fomel et al., 2013) is utilized, but now for the 3D case. This  
364 allows us to recover both displacement and strain data along receivers in the grid. A variable density  
365 is now used to create reflectivity instead of using purely velocity changes to create reflectivity in the  
366 2D case.

#### 367 **3D Modeling of Non-Uniform DAS Acquisition**

368 The wavefield along the fiber is now recorded for the six components of strain (XX, XY, XZ, YY,  
369 YZ, and ZZ). Field DAS data with single fiber, however, does not recover all six components. In-  
370 stead, it only recovers contributions of the wavefield in the direction that it is oriented. We can  
371 project the six components from the synthetic data on to the vector direction of the field fiber loca-  
372 tions to recover the strain in the direction that the fiber is oriented by using Equation 4,

$$\begin{bmatrix} \varepsilon_{ZZ} \\ \varepsilon_{XX} \\ \varepsilon_{YY} \\ \varepsilon_{XY} \\ \varepsilon_{YZ} \\ \varepsilon_{ZX} \end{bmatrix} = \begin{bmatrix} V_Z^2 & V_X^2 & V_Y^2 & 2V_XV_Y & 2V_YV_Z & 2V_ZV_X \end{bmatrix} = \begin{bmatrix} \varepsilon' \end{bmatrix} \quad (4)$$

373 where  $\varepsilon_{ij}$  is the strain in the direction  $ij$ ,  $V_i$  is the vector projection in the  $i$  direction, and  $\varepsilon'$  is

374 the strain in the direction of the fiber.

375 A matrix of fiber vector directions must be created prior to using Equation 4. The fiber endpoints

376 were recorded in the field using a handheld GPS device after the fiber was trenched. The virtual

377 receiver locations along the fiber were then interpolated at 1-meter spacing between these endpoints.

378 Although this gives a good estimate of the x and y coordinates of the fiber, this does not give any

379 information on how deep the fiber was trenched. For this reason, we assume that the fiber was

380 all trenched in the same horizontal plane and there are no dips along the fiber. This simplifies

381 Equation 4 to only have contributions from X and Y.

382 Applying Equation 4 recovers only one value of strain along the fiber. In reality, there are

383 contributions from both X and Y, so the strain matrix should have values at XX, YY, and XY. We

384 can use the adjoint operation to recover a vector projection of the strain value from Equation 4. The

385 adjoint operation shown in Equation 5 returns back to the original PoroTomo coordinate system.

$$\begin{bmatrix} \varepsilon' \\ V_Z^2 \\ V_X^2 \\ V_Y^2 \\ 2V_X V_Y \\ 2V_Y V_Z \\ 2V_Z V_X \end{bmatrix} = \begin{bmatrix} \varepsilon_{ZZ} \\ \varepsilon_{XX} \\ \varepsilon_{YY} \\ \varepsilon_{XY} \\ \varepsilon_{YZ} \\ \varepsilon_{ZX} \end{bmatrix} \quad (5)$$

386 The last attribute of fiber that needs to be modeled is the gauge-length. As discussed earlier  
 387 in this paper, the gauge-length of fiber is related to the wavelength recorded along the fiber and it  
 388 acts as a moving average. The gauge-length in the PoroTomo survey was set at 10-meters, so the  
 389 modeled data,  $d$ , is a matrix multiplication of  $\frac{1}{10}$  for the gauge length, the spatial sampling 1-meter,  
 390 and the raw point data,  $b$ , recorded by the finite difference code (shown in Equation 6, after Lim  
 391 Chen Ning and Sava, 2018).

$$\begin{bmatrix} d_5 \\ d_6 \\ d_7 \\ \vdots \\ d_{n-5} \end{bmatrix} = \frac{1}{10} \begin{bmatrix} 1 & 1 & 1 & 1 & 1 & 1 & 1 & 1 & 1 & 1 & 0 & 0 & 0 & 0 \\ 0 & 1 & 1 & 1 & 1 & 1 & 1 & 1 & 1 & 1 & 1 & 0 & 0 & 0 \\ 0 & 0 & 1 & 1 & 1 & 1 & 1 & 1 & 1 & 1 & 1 & 0 & 0 & 0 \\ 0 & 0 & 0 & \ddots & 0 \\ 0 & 0 & 0 & 0 & 1 & 1 & 1 & 1 & 1 & 1 & 1 & 1 & 1 & 1 \end{bmatrix} \begin{bmatrix} b_5 \\ b_6 \\ b_7 \\ \vdots \\ b_{n-5} \end{bmatrix} \quad (6)$$

## 392 Numerical Modeling

393 It is important to image the faults in detail at Brady's Natural Lab as they are the driving factors  
 394 behind the recharge of the geothermal reservoir. Although Siler and Faulds (2013) would be a good

395 candidate for data modeling, a simpler model is needed to first test the hypothesis of imaging using  
396 the two data types simultaneously. A four layer model with a variety of structures is used as the  
397 density model for the first example (Figure 11). There is a contrast of about 300 g/cc between each  
398 layer to ensure strong reflections.

399 The synthetic images are produced using the same methodology presented in the 2D section.  
400 The results from migrating the DAS data are shown in Figure 12. The results from migrating the  
401 geophone data are shown in Figure 13. A visual reflectivity model shown on the left of both figures  
402 was produced by applying the Laplacian operator on Figure 11 and setting all values to one.

403 At first glance, it seems as if the DAS image does not have any reflectors. It can be compared  
404 to the true reflectivity model shown on the right of Figure 12 to identify the signal **true horizons** in  
405 the image. It is clear that the data recorded by the DAS fiber is too low in frequency to resolve the  
406 beds within the image. This is due to both the velocity field that the experiment used to mimic the  
407 PoroTomo subsurface and the FDM accuracy condition presented in Equation 7.

$$\frac{v_{min}}{f_{max}} > N * \sqrt{dx^2 + dy^2 + dz^2} \quad (7)$$

408 The minimum velocity of approximately 950 m/s from the input velocity field forces the maxi-  
409 mum frequency of the wavelet to be 16 Hz and the peak frequency of the wavelet to be 12 Hz. This  
410 equates to a 12 Hz wavelet and the velocity model corresponds to a wavelength of about 108 meters.

411 The DAS image (Figure 12) is also contaminated by fake modes and migration artifacts (Rocha  
412 et al., 2016). Fake modes are expected since the displacement field is incomplete when wavefield  
413 extrapolation was performed as the fiber is only recording one component of strain in the direction  
414 that it is oriented. An inexperienced interpreter would eagerly interpret the fake modes as an area

415 of interest for further exploration methods.

416 At first glance, the geophone data also appear to have no clear reflection events. The image can  
417 again be compared to the true reflectivity model overlain on the left of Figure 13 to identify the  
418 signal **true horizons** in the image. The geophone image is also limited by the source wavelet that  
419 was injected into the model. Differentiation between the thin beds is not possible using the source  
420 wavelet in this experiment.

421 The geophone image, similar to the DAS image, is also contaminated by migration artifacts.  
422 These migration artifacts, however, are due to the insufficient sampling that creates migration ar-  
423 tifacts on the edge of reflectors. The wavefield is not sampled completely because the geophones  
424 adopted from the PoroTomo survey are placed sparsely around the model (the average geophone  
425 spacing is about 80 meters).

## 426 Quantitative Image Comparison

427 In 2D, a machine learning methodology was used to create a quantitative image comparison. Al-  
428 though 3D CNN's exist, they are not as polished and readily available as are 2D CNN's. Instead, the  
429 data are quantitatively analyzed using energy norm image filtering. Energy norm filtering focuses  
430 on highlighting areas with reflected energy is maximum, so filtering the image based on an applied  
431 limit will highlight where reflections may be coming from as opposed to migration artifacts. The  
432 geophone and DAS images are combined by first normalizing the data types based on their maxi-  
433 mum amplitude. They are then stacked together to test this hypothesis. This image would ideally  
434 highlight continuous reflectors with the densely sampled DAS data and reduce migration artifacts  
435 by extrapolating the full displacement wavefield with the multi-component geophones.

436 Every model cell that is above an applied limit is assigned a value of 1 and every model box that

Table 1: Confusion matrix for top 90% energy reflected.

Top 90% energy reflected		
	$\theta_R^{int}$	$\theta_{NR}^{int}$
$\theta_R$	184800	1206000
$\theta_{NR}$	346700	1824000

is below the limit is assigned a value of 0. A cell-by-cell comparison between the filtered, multi-component geophone image and the original reflectivity model is performed to identify how much additional accuracy is gained by adding the DAS data. The results of this cell-by-cell comparison are presented in confusion matrix form (Table 1), where  $R$  represents reflections and  $NR$  represents not reflections.

The confusion matrices assist in calculating the posterior value using Equation 3. The posterior value explains the probability that an event which the data type predicted is the event present. The posterior can then be used to calculate the utility or value of information added when using DAS and geophone versus only geophone with Equation 1. The results for the medium filter, posterior values in the four layer model presented in this paper are displayed in Figure 14.

In this experiment, adding distributed sensors increases the probability of finding if a cell is not a reflector and decreases the probability of false negatives. Adding distributed sensors, however, increases the probability of identifying false positives and decreases the probability of finding true reflectors. This experiment, however, is inconclusive in identifying if DAS has added value with sparsely sampled arranged geophone data. A better DAS geometry must be tested to make further conclusions on the effectiveness of surface DAS fiber.

The geometry shown in Figure 15 is utilized to further test the effectiveness of surface DAS fiber. This new acquisition utilizes 25% less fiber and 60% fewer sources than the PoroTomo survey

455 geometry. Quantitative analysis using the energy norm filtering methodology is utilized again to  
456 identify how well the survey imaged. The results are presented in Figure 16

457 Figure 16 shows a significant increase in true positives and decrease in false negatives. Al-  
458 though there was an increase in false positives and a decrease in true negatives, the increase in true  
459 positives proves that this new acquisition is better suited to image the subsurface with surface DAS  
460 fibers. Energy norm imaging again allowed for an automatic method to interpret images output  
461 from the migration images. Filtering images based on amplitudes is a crude approximation of how  
462 an interpreter would “interpret” an image.

463 **3D Summary**

464 This section discussed differences in modeling DAS data in 3D versus 2D. The experiments in this  
465 section helped clarify what kinds of data that a single surface DAS fiber can record. The experiments  
466 discovered that the DAS configuration in the PoroTomo survey combined with the low frequency  
467 nature of the modeling did not add value to the multi-component geophone imaging effort. Addi-  
468 tionally, the percentages of missing strain components in 3D is larger than the 2D case, contributing  
469 to the poor image quality. A better geometry and multi-component DAS were required to make  
470 further conclusions on the effectiveness of DAS fiber in surface acquisition. Another experiment  
471 was preformed with DAS fibers arranged in 2D lines. This acquisition geometry led to an increased  
472 percentage of reflectors identified. It is concluded that the 2D surface DAS fiber lines are a better  
473 suited geometry to image the subsurface.

## CONCLUSIONS

474 In this paper, we discussed some of the fiber attributes that are essential to understand before looking  
475 at surface DAS data. The most important attribute is the types of waves that fiber is directionally  
476 sensitive. It is concluded that surface DAS in a flat-layered Earth model is sensitive to long offset  
477 P-waves, short offset SV-waves, and SH-waves produced by a source that is perpendicular to the  
478 fiber orientation.

479 It was discovered that the geophone data in the PoroTomo survey was too sparsely sampled  
480 arranged, and the hypothesis that densely sampled DAS data DAS, which samples the Earth's re-  
481 sponse well, can fill in the gaps of the geophones was introduced. This hypothesis was tested in  
482 2D using elastic numerical modeling and RTM. It is then shown how data are modeled for DAS  
483 receivers in 2D. The energy norm imaging condition was chosen as it allowed for an easier method  
484 to compare two images than the conventional imaging condition. The experiments showed that  
485 an inline horizontal force allows for the best results qualitatively due to the resulting SV reflec-  
486 tions. Lastly, this section explains the need for statistical and quantitative analysis in the geophysics  
487 realm. A description of how to perform quantitative analysis using machine learning methodology  
488 is presented. Both methods concluded that DAS added imaging value to sparsely sampled multi-  
489 component geophones.

490 The 2D scenario did not test the full DAS fiber directionality. We discuss 3D numerical mod-  
491 eling and RTM used to combine DAS and multi-component geophone data. The challenges of  
492 modeling DAS in 3D are also discussed including recording the proper component of strain along  
493 the fiber. The resulting migrated images did not clarify if DAS added any qualitative value to multi-  
494 component geophone images as the migrated images were too low of a frequency to analyze due  
495 to the limitation of the velocity model. A quantitative analysis of the combined image is utilized.

496 This chapter concluded that adding DAS data only helped to reduce the number of false positives  
497 by a very small fraction. This experiment is inconclusive in regards to identifying if DAS can add  
498 value to sparsely sampled geophone data, so another experiment was performed with 2D surface  
499 DAS fiber lines. The new proposed experiment with long-offset, 2D surface fiber lines concluded  
500 that using the new geometry was better suited for surface DAS acquisitions. The next proposed step  
501 is to test this hypothesis with field data.

## REFERENCES

- 502 Aki, K., and P. G. Richards, 1980, Quantative seismology: Theory and methods: New York, **801**.
- 503 Barberan, C., C. Allanic, D. Avila, J. Hy-Billiot, A. Hartog, B. Frignet, and G. Lees, 2012, Multi-
- 504 offset seismic acquisition using optical fiber behind tubing: Presented at the 74th EAGE Confer-
- 505 ence and Exhibition incorporating EUROPEC 2012.
- 506 Cardiff, M., D. D. Lim, J. R. Patterson, J. Akerley, P. Spielman, J. Lopeman, P. Walsh, A. Singh, W.
- 507 Foxall, H. F. Wang, et al., 2018, Geothermal production and reduced seismicity: Correlation and
- 508 proposed mechanism: Earth and Planetary Science Letters, **482**, 470–477.
- 509 Claerbout, J. F., 1985, Imaging the earth's interior: Blackwell scientific publications Oxford, **1**.
- 510 Clarke, R., and C. L. Sandberg, 1983, Fiber optic temperature sensing. (US Patent 4,417,782).
- 511 Cox, B., P. Wills, D. Kiyashchenko, J. Mestayer, J. Lopez, S. Bourne, R. Lupton, G. Solano, N.
- 512 Henderson, D. Hill, et al., 2012, Distributed acoustic sensing for geophysical measurement, mon-
- 513 itoring and verification: **37**, 7–13.
- 514 Daley, T., D. Miller, K. Dodds, P. Cook, and B. Freifeld, 2015, Field testing of modular borehole
- 515 monitoring with simultaneous distributed acoustic sensing and geophone vertical seismic profiles
- 516 at citronelle, alabama: Geophysical Prospecting.
- 517 Daley, T. M., B. M. Freifeld, J. Ajo-Franklin, S. Dou, R. Pevzner, V. Shulakova, S. Kashikar, D. E.
- 518 Miller, J. Goetz, J. Henninges, et al., 2013, Field testing of fiber-optic distributed acoustic sensing
- 519 (das) for subsurface seismic monitoring: The Leading Edge, **32**, 699–706.
- 520 Feigl, K. L., 2017, Overview and preliminary results from the porotomo project at brady hot springs,
- 521 nevada: Poroelastic tomography by adjoint inverse modeling of data from seismology, geodesy,
- 522 and hydrology: Presented at the Stanford Geothermal Workshop.
- 523 Folsom, M., J. Lopeman, D. Perkin, and M. Sophy, 2018, Imaging shallow outflow alteration to
- 524 locate productive faults in ormats bradys and desert peak fields using csamt.

- 525 Fomel, S., P. Sava, I. Vlad, Y. Liu, and V. Bashkardin, 2013, Madagascar: Open-source software  
526 project for multidimensional data analysis and reproducible computational experiments: Journal  
527 of Open Research Software, **1**.
- 528 Gerven, M. V., and S. Bohte, 2018, Artificial Neural Networks as Models of Neural Information  
529 Processing.
- 530 Hornman, J., 2017, Field trial of seismic recording using distributed acoustic sensing with broadside  
531 sensitive fibre-optic cables: Geophysical Prospecting, **65**, 35–46.
- 532 Hornman, K., B. Kuvshinov, P. Zwartjes, and A. Franzen, 2013, Field trial of a broadside-sensitive  
533 distributed acoustic sensing cable for surface seismic: Presented at the 75th EAGE Conference  
534 & Exhibition incorporating SPE EUROPEC 2013.
- 535 Jreij, S., W. Trainor-Guitton, D. Miller, et al., 2017, Field data comparison of 3d horizontal dis-  
536 tributed acoustic sensing and geophones: SEG Technical Program Expanded Abstracts.
- 537 Krohn, D. A., T. MacDougall, and A. Mendez, 2000, Fiber optic sensors: fundamentals and appli-  
538 cations: Isa.
- 539 Lindsey, N. J., E. R. Martin, D. S. Dreger, B. Freifeld, S. Cole, S. R. James, B. L. Biondi, and J. B.  
540 Ajo-Franklin, 2017, Fiber-optic network observations of earthquake wavefields: Geophysical  
541 Research Letters.
- 542 Mateeva, A., J. Lopez, J. Mestayer, P. Wills, B. Cox, D. Kiyashchenko, Z. Yang, W. Berlang, R.  
543 Detomo, and S. Grandi, 2013, Distributed acoustic sensing for reservoir monitoring with vsp:  
544 The Leading Edge, **32**, 1278–1283.
- 545 Mateeva, A., J. Lopez, H. Potters, J. Mestayer, B. Cox, D. Kiyashchenko, P. Wills, S. Grandi, K.  
546 Hornman, B. Kuvshinov, et al., 2014, Distributed acoustic sensing for reservoir monitoring with  
547 vertical seismic profiling: Geophysical Prospecting, **62**, 679–692.
- 548 Matzel, E., X. Zeng, C. Thurber, Y. Luo, C. Morency, et al., 2017a, Seismic interferometry using

549 the dense array at the brady geothermal field.

550 Matzel, E. M., X. Zeng, C. Thurber, and C. Morency, 2017b, Using Virtual Earthquakes to Charac-

551 terize the Material Properties of the Brady Hot Springs , Nevada: Geothermal Resources Council.

552 Mestayer, J., B. Cox, P. Wills, D. Kiyashchenko, J. Lopez, M. Costello, S. Bourne, G. Ugueto,

553 R. Lupton, G. Solano, et al., 2011, Field trials of distributed acoustic sensing for geophysical

554 monitoring, *in* SEG Technical Program Expanded Abstracts 2011: Society of Exploration Geo-

555 physists, 4253–4257.

556 Parker, T., S. Shatalin, and M. Farhadiroushan, 2014, Distributed Acoustic Sensing - A new tool for

557 seismic applications: First Break, **32**, 61–69.

558 Rocha, D., N. Tanushev, and P. Sava, 2016, Isotropic elastic wavefield imaging using the energy

559 norm: Geophysics, **81**, S207–S219.

560 Russakovsky, O., J. Deng, H. Su, J. Krause, S. Satheesh, S. Ma, Z. Huang, A. Karpathy, A. Khosla,

561 M. Bernstein, A. C. Berg, and L. Fei-Fei, 2015, ImageNet Large Scale Visual Recognition Chal-

562 lenge: International Journal of Computer Vision (IJCV), **115**, 211–252.

563 Samuel, A. L., 1959, Some studies in machine learning using the game of checkers: IBM Journal

564 of research and development, **3**, 210–229.

565 Siler, D. L., and J. E. Faulds, 2013, Three-dimensional geothermal fairway mapping: Examples

566 from the western great basin, usa,: GRC Transactions, **7**, 327–332.

567 Szegedy, C., V. Vanhoucke, S. Ioffe, J. Shlens, and Z. Wojna, 2015, Rethinking the Inception Ar-

568 chitecture for Computer Vision.

569 Trainor-Guitton, W. J., A. Ramirez, X. Yang, K. Mansoor, Y. Sun, and S. Carroll, 2013, Value

570 of information methodology for assessing the ability of electrical resistivity to detect co2/brine

571 leakage into a shallow aquifer: International Journal of Greenhouse Gas Control, **18**, 101–113.

## LIST OF FIGURES

572        1      PoroTomo survey geometry. Green dots represent source locations, red dots represent geo-

573      phone locations, and the blue line represents the surface DAS layout.

574        2      Consider a source that generates both P and S waves; this is a 2D Homogeneous, flat-

575      layered, isotropic ray path example. The blue lines represent ray paths of the labeled waves, the

576      blue arrow represents the propagation direction of the wave, the green line represents a horizontal

577      reflector in the subsurface, and the yellow star represents the source. (a) Demonstration of P-P wave

578      effect on the fiber using ray paths. Particle motion is inline with propagation direction (blue arrow).

579      The fiber will only record data at large offsets. (b) Demonstration of SV-SV wave effect on the fiber

580      using ray paths. Particle motion is perpendicular with the propagation direction (green arrows). The

581      fiber will only record data at short offsets.

582        3      Amplitude versus emerging angle for both geophone (blue) and horizontal DAS (red). An

583      emerging angle of  $0^\circ$  indicates a wave that is propagating perpendicular to the surface and an emerg-

584      ing angle of  $90^\circ$  degrees indicated a wave is propagating parallel to the surface. (a) Sensitivity with

585      respect to a P-wave at different emerging angles of horizontal DAS (red) and geophone z-component

586      (blue). (b) Sensitivity with respect to an SV-wave at different emerging angles of horizontal DAS

587      (red) and geophone x-component (blue).

588        4      Siler and Faulds (2013) fault density mapping within the PoroTomo Survey box. This

589      model was used as a reflectivity model for the experiments within this section.

590        5      Reflectivity model from Siler and Faulds (2013) extracted at the location of Well 56-A1

591      used for simulating data. Blue dots represent source locations and the red dots represent geophone

592      locations. DAS fiber was placed between the geophone locations.

593        6      (a) Resulting image from migrating geophone synthetic data. (b) Resulting image from

594      migrating DAS synthetic data. (c) Combined image from migrating DAS and geophone synthetic

595 data.

596 7 (a) Resulting image from migrating geophone synthetic data. (b) Resulting image from  
597 migrating DAS synthetic data. (c) Combined image from migrating DAS and geophone synthetic  
598 data.

599 8 (a) Examples of the automatically generated faults images used to train the CNN. (b) Ex-  
600 amples of the automatically generated images that were not faults used to train the CNN.

601 9 Posterior reliability of information from CNN's calculated using Equation 3 using (a) a  
602 vertical force and (b) a horizontal force. The objective is to maximize the percentages of true posi-  
603 tives and negatives (green arrows) while minimizing the percentages of false positives and negatives  
604 (red arrows). This is obtained by having better instruments as well as better classification.

605 10 Body wave (P-wave) velocity (m/s) model from sweep interferometry in 3D perspective  
606 (Matzel et al., 2017b).

607 11 Four layer model with a variety of structures used for data modeling. This model is used  
608 as a density model for elastic modeling.

609 12 Results of migrating the reflectivity model (Figure 11) using the PoroTomo DAS acquisi-  
610 tion shown on the right. The true reflectivity model is overlain and shown on the left. The slices on  
611 each side are taken at the yellow cross shown on the map view of the acquisition.

612 13 Results of migrating the reflectivity model (Figure 11) using the PoroTomo geophone ac-  
613 quisition shown on the right. The true reflectivity model is overlain and shown on the left. The  
614 slices on each side are taken at the yellow cross shown on the map view of the acquisition.

615 14 Posterior reliability of information from energy norm filtering calculated using Equation 3  
616 using a horizontal force. The objective is to maximize the percentages of true positives and nega-  
617 tives (green arrows) while minimizing the percentages of false positives and negatives (red arrows).

618 15 New survey geometry proposed to test the effectiveness of surface DAS fiber. Green dots

619 represent source locations, red dots represent geophone locations, and the blue lines represent the  
620 surface DAS acquisition.

621 16 Posterior reliability of information using a horizontal force and the Figure 15 acquisition  
622 geometry.

623

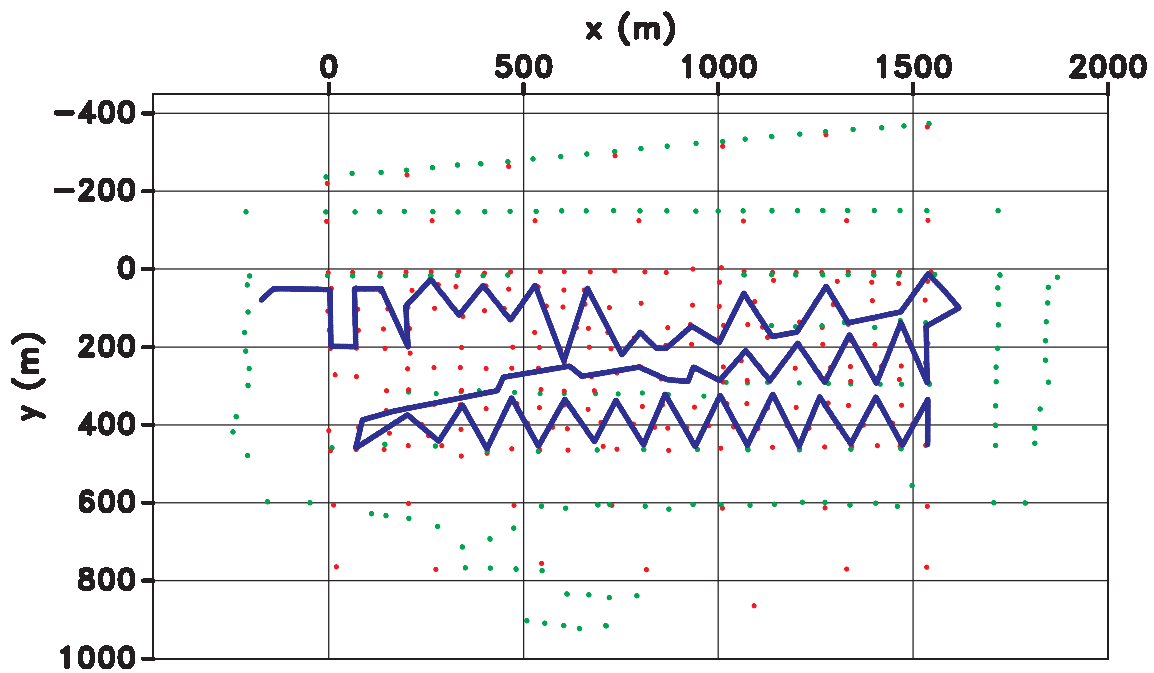
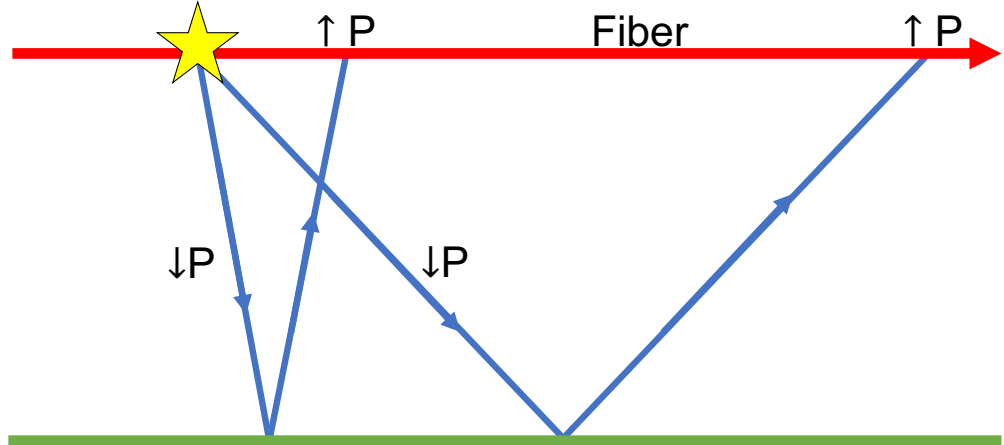
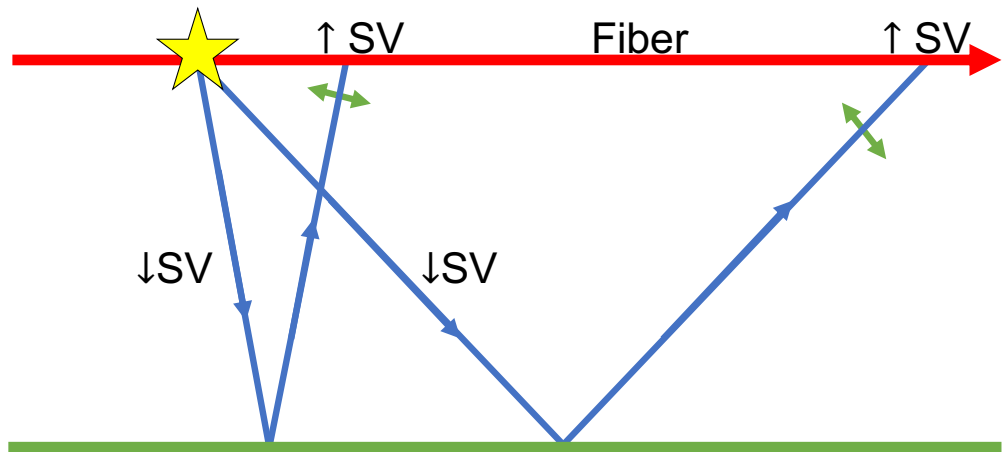


Figure 1: PoroTomo survey geometry. Green dots represent source locations, red dots represent geophone locations, and the blue line represents the surface DAS layout.



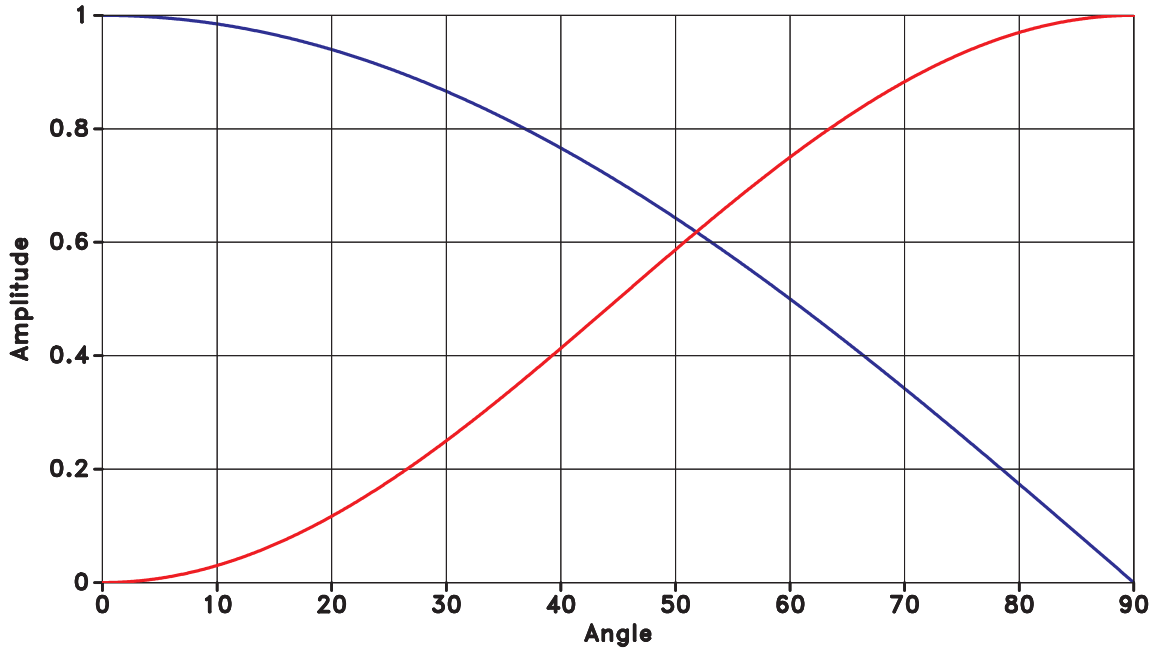
(a)



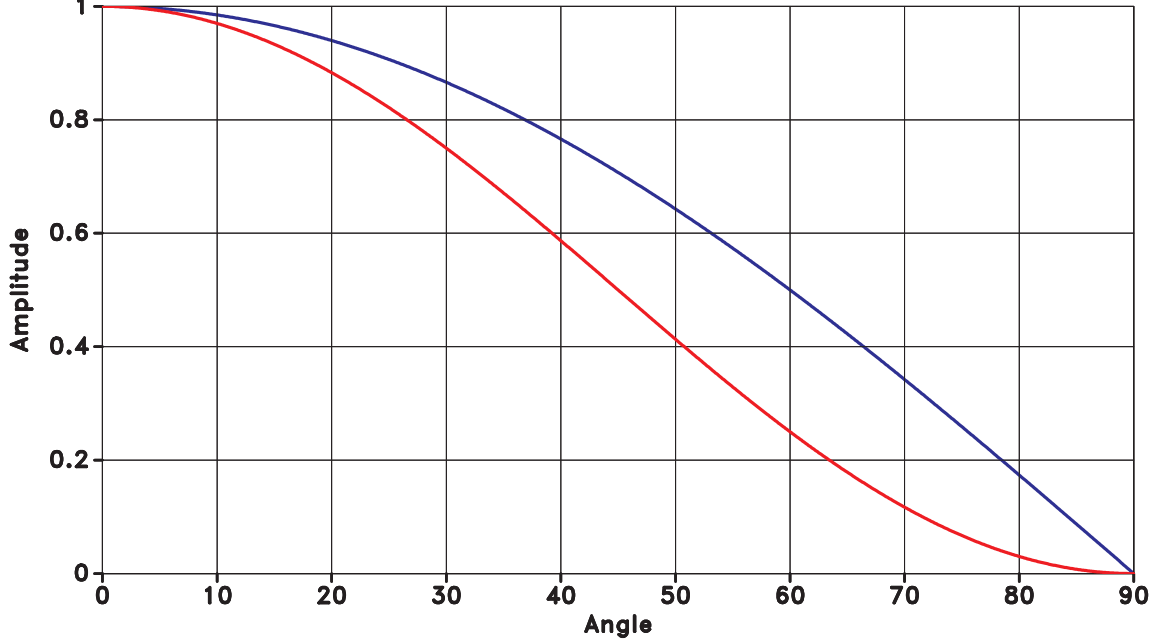
(b)

Figure 2: Consider a source that generates both P and S waves; this is a 2D Homogeneous, flat-layered, isotropic ray path example. The blue lines represent ray paths of the labeled waves, the blue arrow represents the propagation direction of the wave, the green line represents a horizontal reflector in the subsurface, and the yellow star represents the source. (a) Demonstration of P-P wave effect on the fiber using ray paths. Particle motion is inline with propagation direction (blue arrow). The fiber will only record data at large offsets. (b) Demonstration of SV-SV wave effect on the fiber using ray paths. Particle motion is perpendicular with the propagation direction (green arrows). The fiber will only record data at short offsets.

-



(a)



(b)

Figure 3: Amplitude versus emerging angle for both geophone (blue) and horizontal DAS (red). An emerging angle of  $0^\circ$  indicates a wave that is propagating perpendicular to the surface and an emerging angle of  $90^\circ$  degrees indicated a wave is propagating parallel to the surface. (a) Sensitivity with respect to a P-wave at different emerging angles of horizontal DAS (red) and geophone z-component (blue). (b) Sensitivity with respect to an SV-wave at different emerging angles of horizontal DAS (red) and geophone x-component (blue).

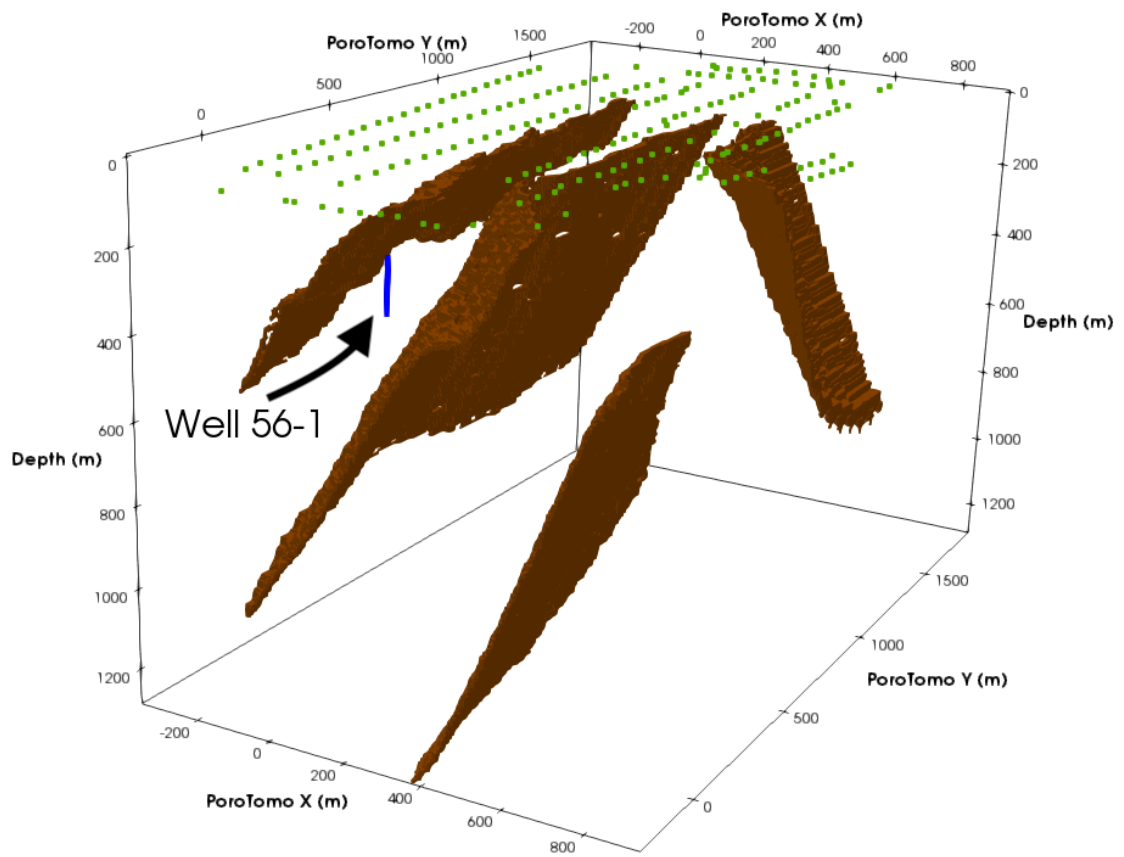


Figure 4: Siler and Faulds (2013) fault density mapping within the PoroTomo Survey box. This model was used as a reflectivity model for the experiments within this section.

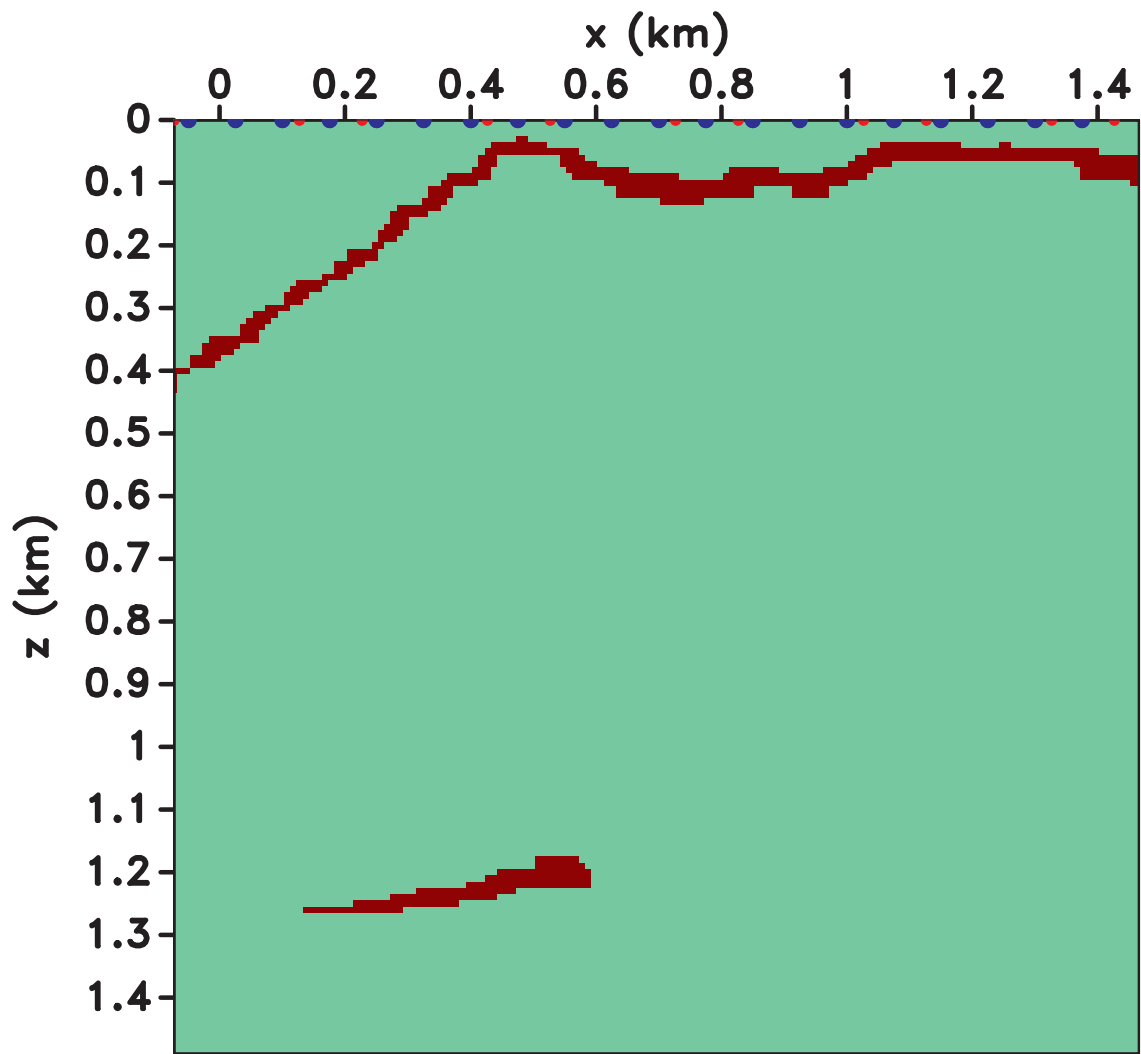


Figure 5: Reflectivity model from Siler and Faulds (2013) extracted at the location of Well 56-A1 used for simulating data. Blue dots represent source locations and the red dots represent geophone locations. DAS fiber was placed between the geophone locations.

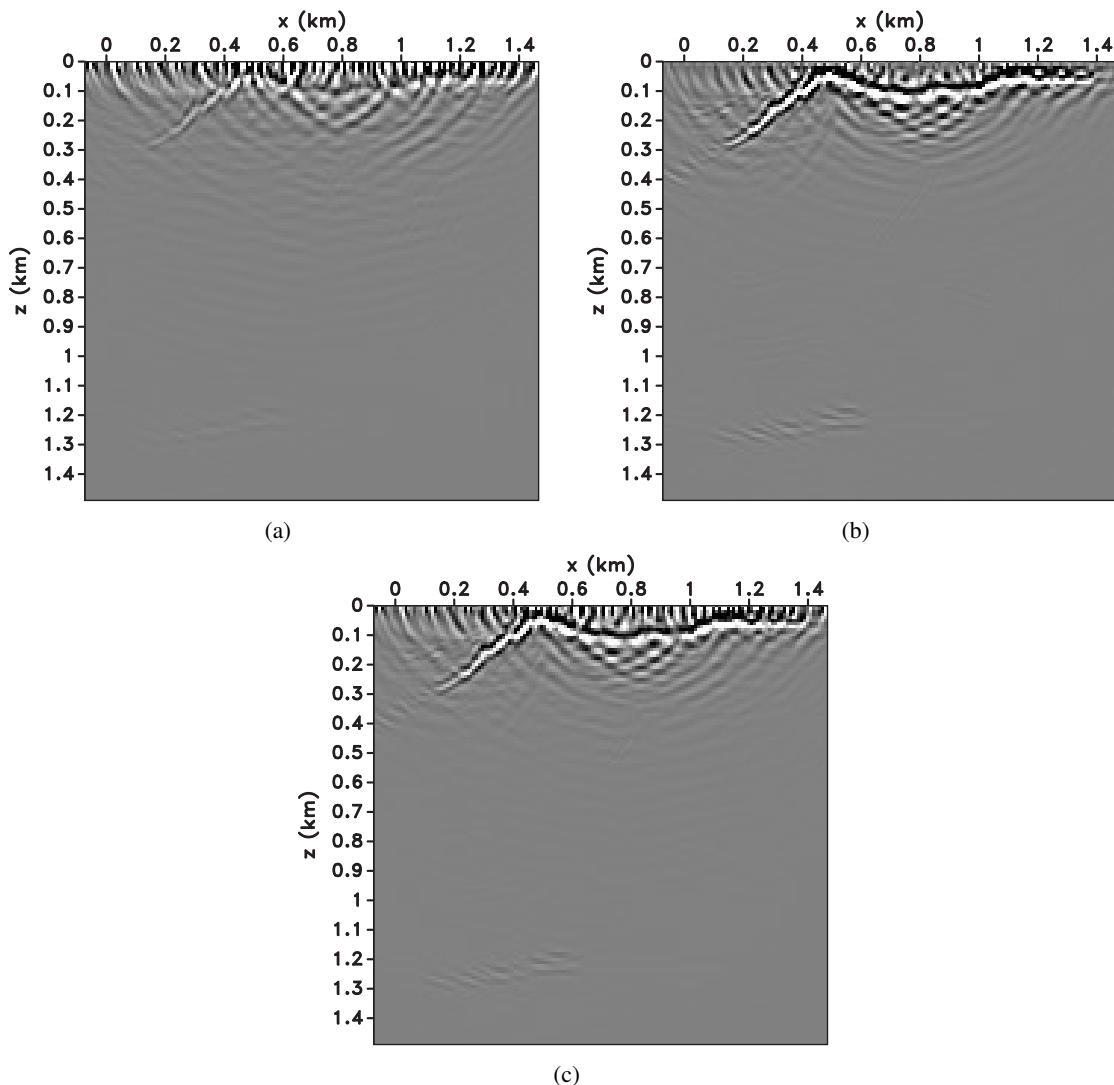


Figure 6: (a) Resulting image from migrating geophone synthetic data. (b) Resulting image from migrating DAS synthetic data. (c) Combined image from migrating DAS and geophone synthetic data.

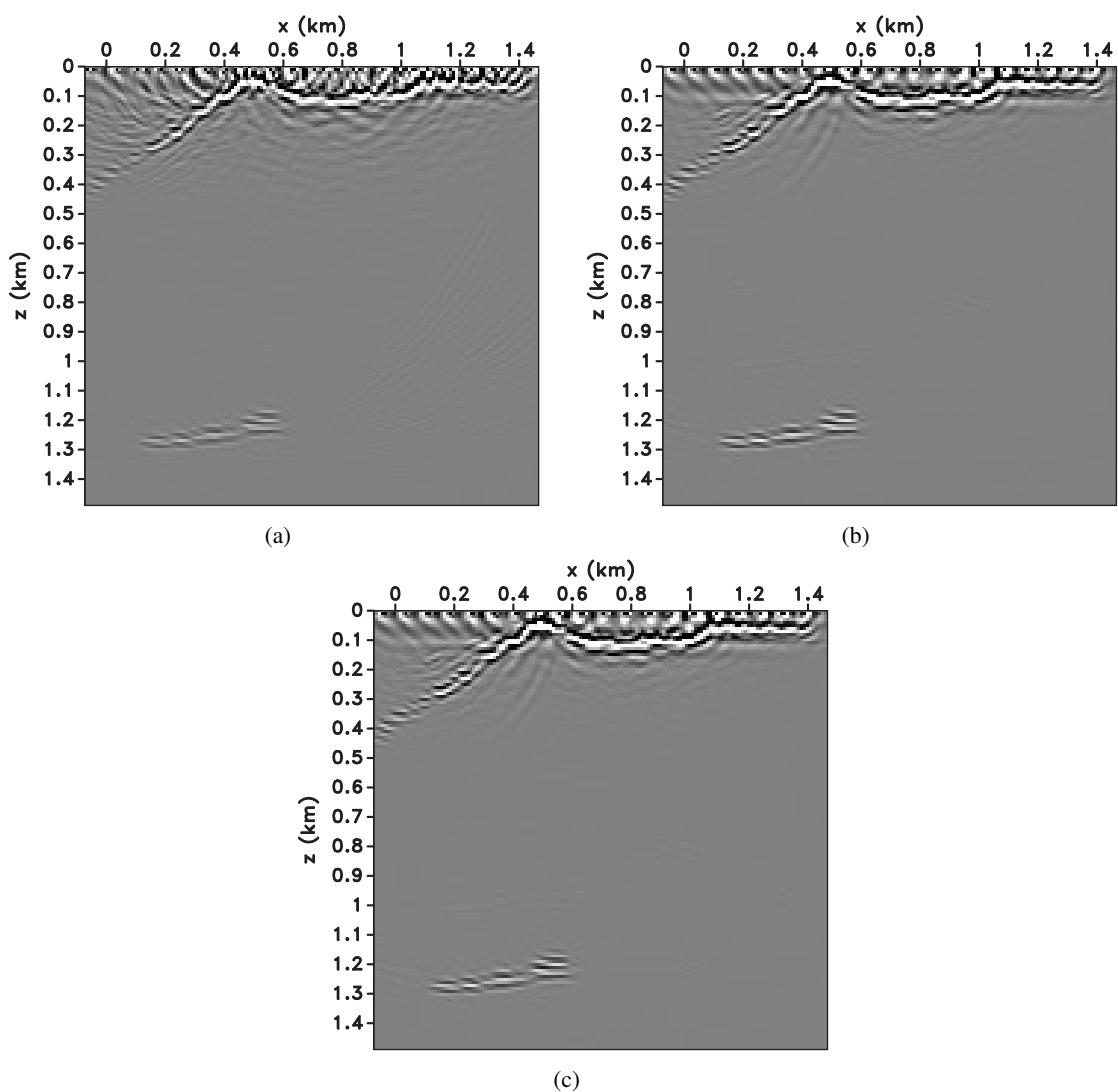


Figure 7: (a) Resulting image from migrating geophone synthetic data. (b) Resulting image from migrating DAS synthetic data. (c) Combined image from migrating DAS and geophone synthetic data.

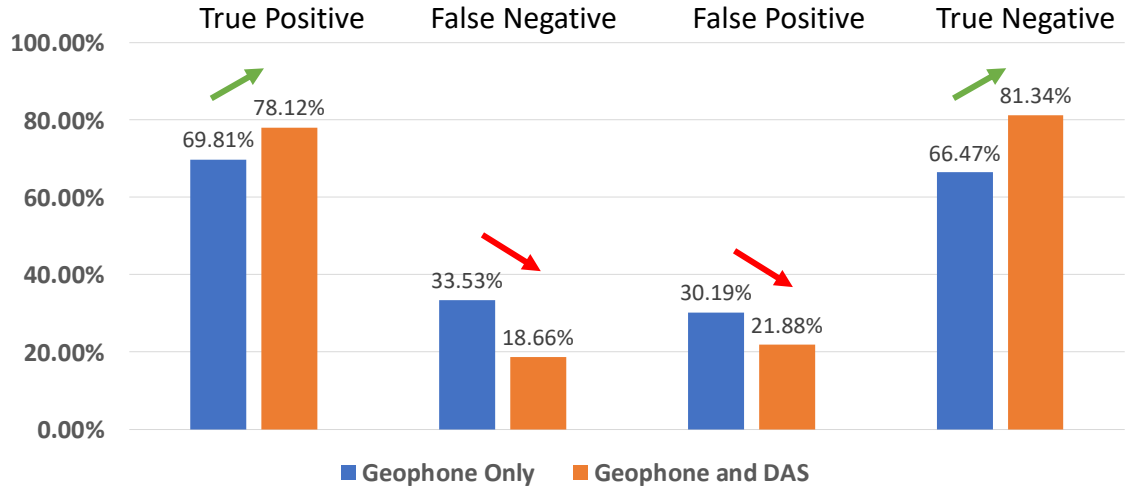


(a)

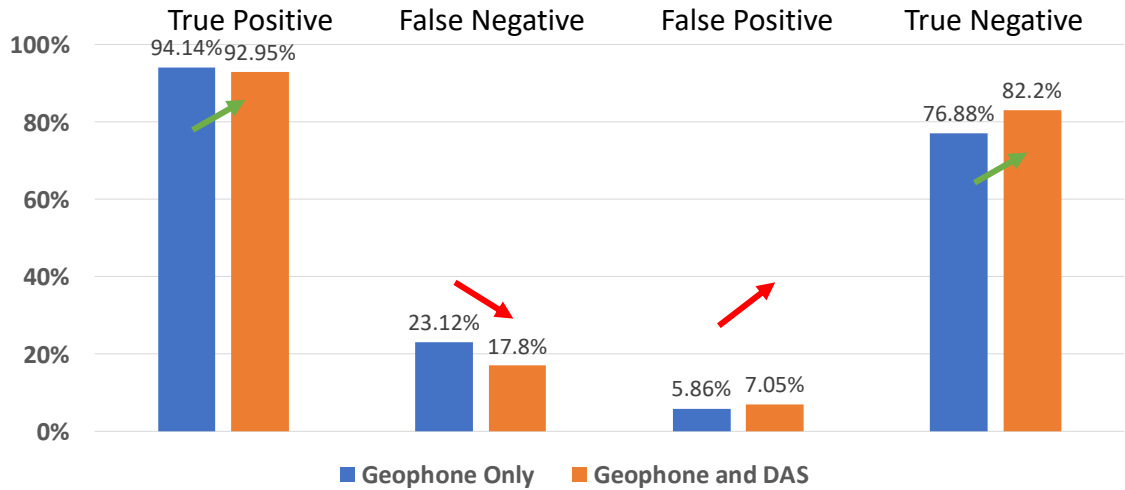


(b)

Figure 8: (a) Examples of the automatically generated faults images used to train the CNN. (b) Examples of the automatically generated images that were not faults used to train the CNN.



(a)



(b)

Figure 9: Posterior reliability of information from CNN's calculated using Equation 3 using (a) a vertical force and (b) a horizontal force. The objective is to maximize the percentages of true positives and negatives (green arrows) while minimizing the percentages of false positives and negatives (red arrows). This is obtained by having better instruments as well as better classification.

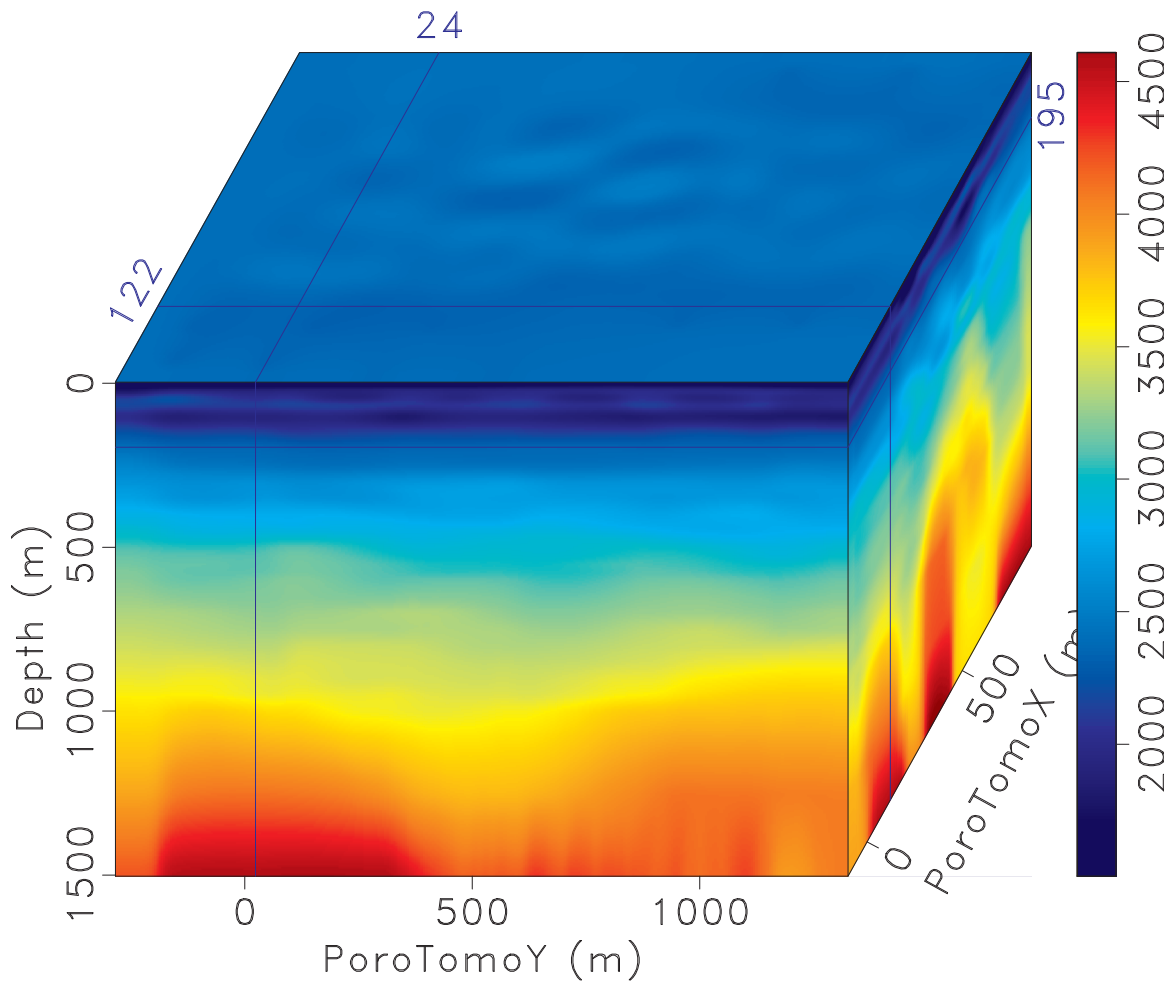


Figure 10: Body wave (P-wave) velocity (m/s) model from sweep interferometry in 3D perspective (Matzel et al., 2017b).

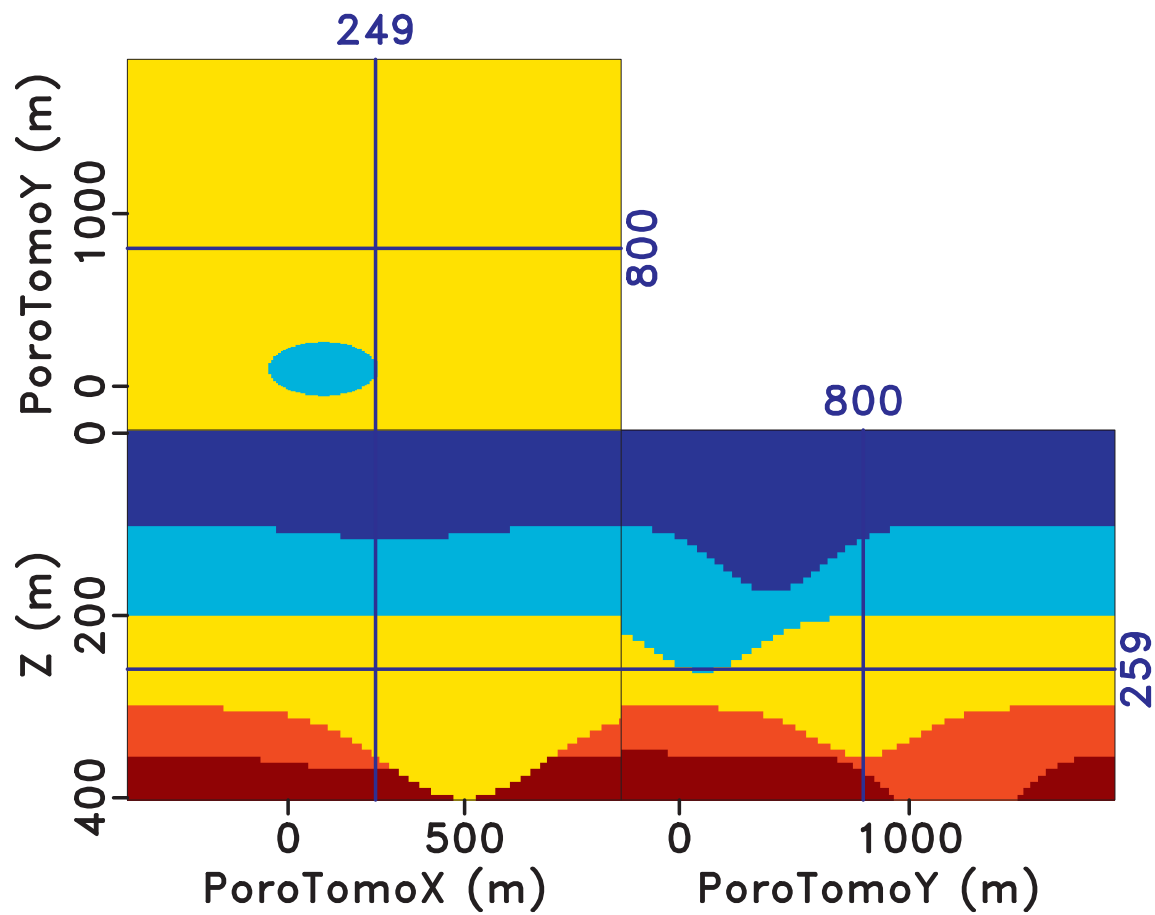


Figure 11: Four layer model with a variety of structures used for data modeling. This model is used as a density model for elastic modeling.

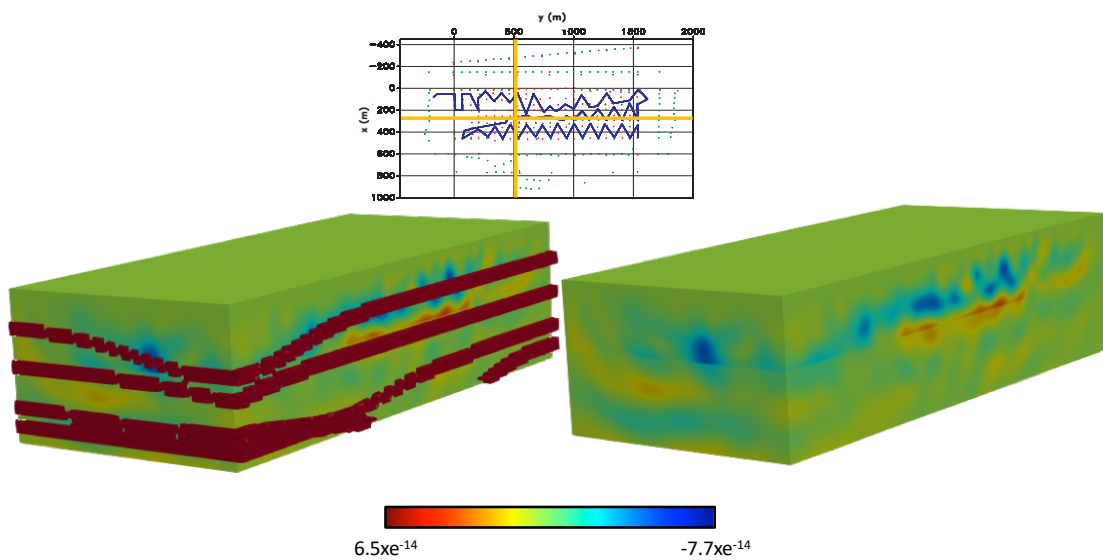


Figure 12: Results of migrating the reflectivity model (Figure 11) using the PoroTomo DAS acquisition shown on the right. The true reflectivity model is overlain and shown on the left. The slices on each side are taken at the yellow cross shown on the map view of the acquisition.

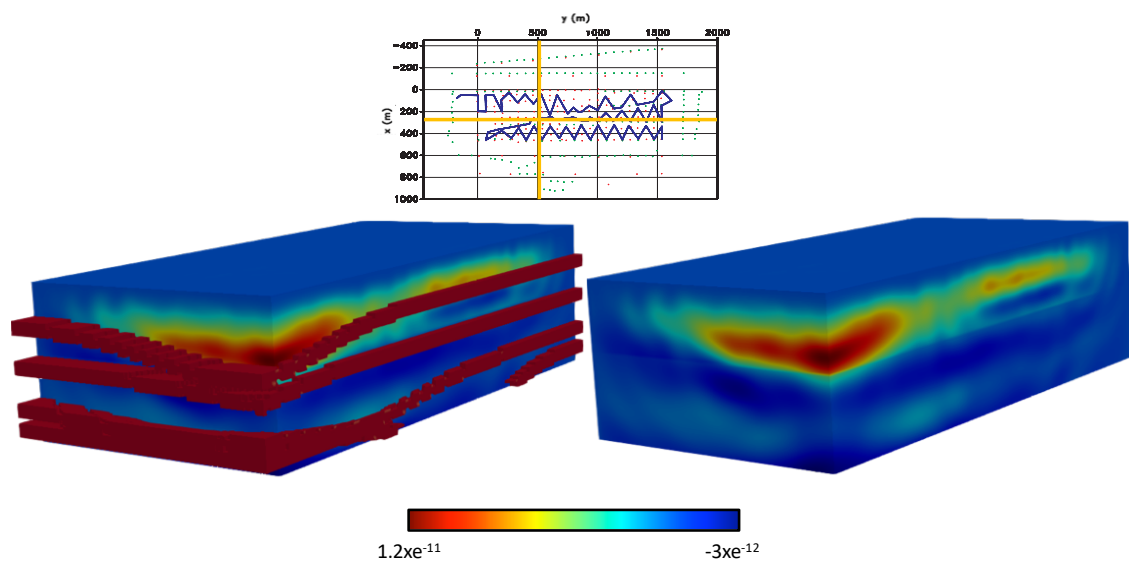


Figure 13: Results of migrating the reflectivity model (Figure 11) using the PoroTomo geophone acquisition shown on the right. The true reflectivity model is overlain and shown on the left. The slices on each side are taken at the yellow cross shown on the map view of the acquisition.

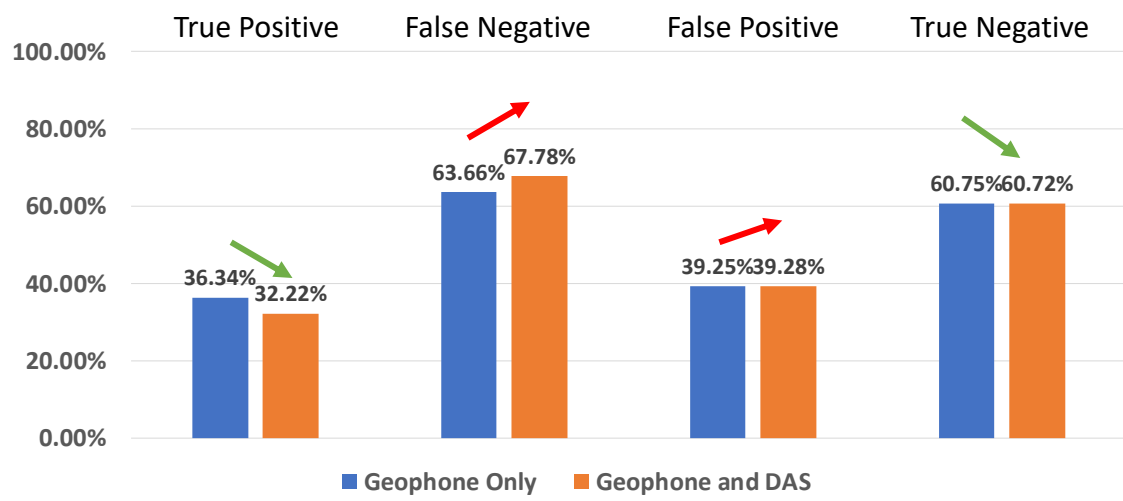


Figure 14: Posterior reliability of information from energy norm filtering calculated using Equation 3 using a horizontal force. The objective is to maximize the percentages of true positives and negatives (green arrows) while minimizing the percentages of false positives and negatives (red arrows).

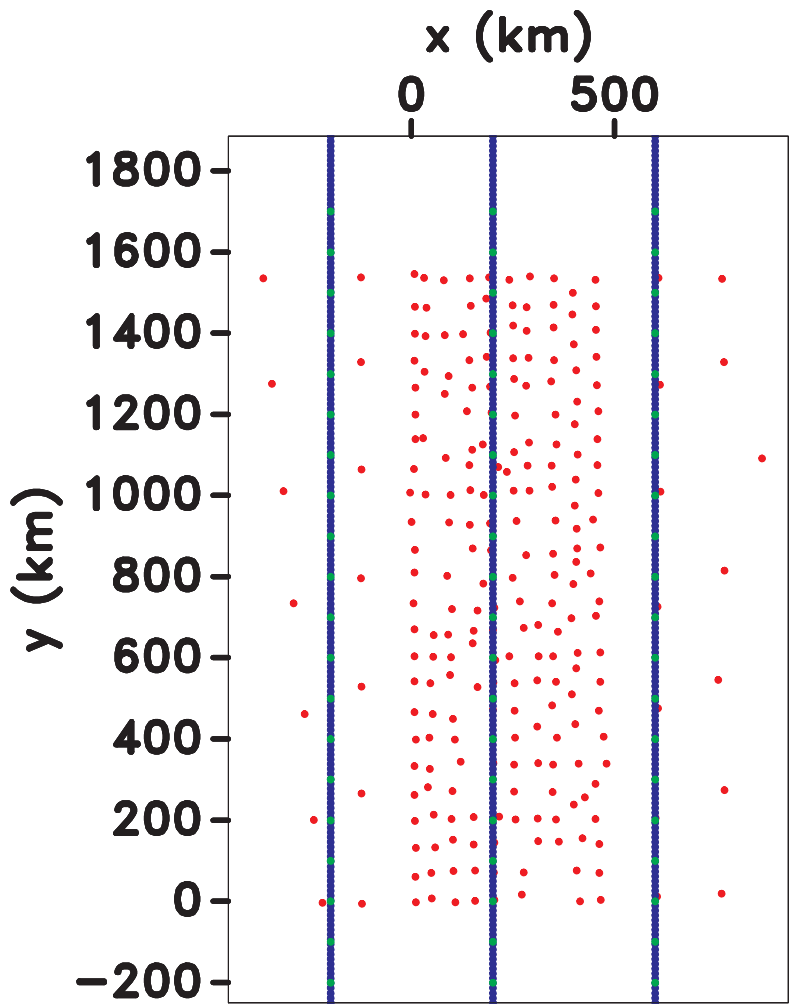


Figure 15: New survey geometry proposed to test the effectiveness of surface DAS fiber. Green dots represent source locations, red dots represent geophone locations, and the blue lines represent the surface DAS acquisition.

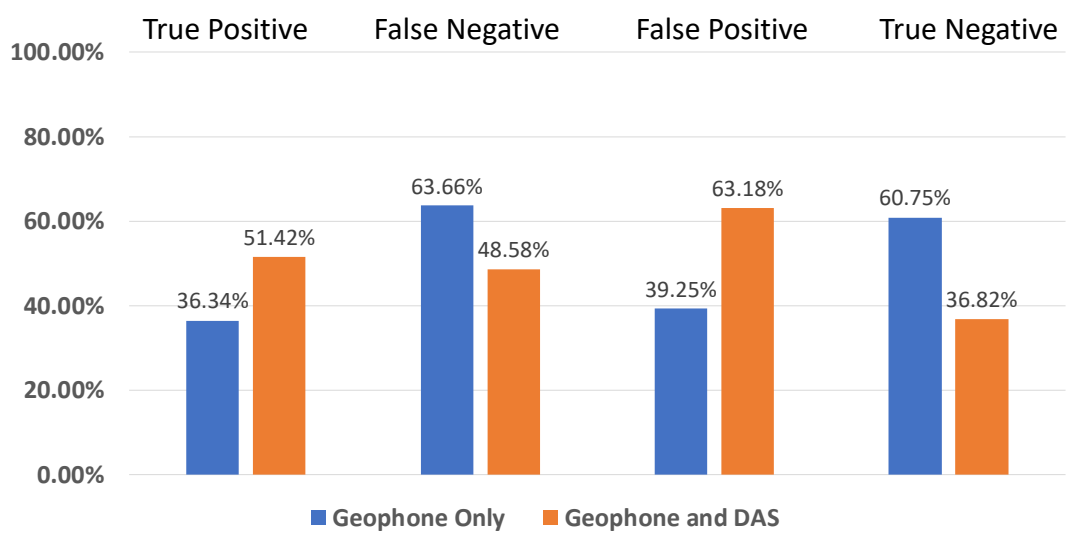


Figure 16: Posterior reliability of information using a horizontal force and the Figure 15 acquisition geometry.